

Doublon-holon origin of the subpeaks at the Hubbard band edges

Seung-Sup B. Lee, Jan von Delft, and Andreas Weichselbaum

Physics Department, Arnold Sommerfeld Center for Theoretical Physics and Center for NanoScience,
Ludwig-Maximilians-Universität München, Theresienstraße 37, 80333 München, Germany

(Dated: December 16, 2022)

Dynamical mean-field theory (DMFT) studies frequently observe a fine structure in the local spectral function of the SU(2) Fermi-Hubbard model at half filling: in the metallic phase close to the Mott transition, subpeaks emerge at the inner edges of the Hubbard bands. Here we demonstrate that these subpeaks originate from the low-energy effective interaction of doublon-holon pairs, by investigating how the correlation functions of doublon and holon operators contribute to the subpeaks. DMFT calculations using the numerical renormalization group (NRG) as an impurity solver and a mean-field analysis of the low-energy effective Hamiltonian provide consistent results. In the SU(3) and SU(4) Hubbard models, the subpeaks become more pronounced due to the increased degeneracy of doublon-holon pair excitations.

Introduction.— Dynamical mean-field theory (DMFT) [1] provides a widely successful approach in understanding strongly correlated systems. It treats a lattice problem by self-consistently solving an effective impurity model whose impurity and bath correspond to a lattice site and the rest of the lattice, respectively. Thus the performance of DMFT calculations directly depends on which particular impurity solver is chosen.

A benchmark calculation for various impurity solvers is the paramagnetic Mott transition in the half-filled SU(2) Hubbard model at temperature $T = 0$ which is characterized by a striking change in the local spectral functions [2, 3]. In the metallic phase, the spectral function features a quasiparticle peak (QP) at the Fermi level, and two Hubbard bands (HBs) below and above the Fermi level each. In the insulating phase, the QP disappears and a gap opens between two HBs.

In the metallic phase close to the transition, many DMFT studies have observed sharp subpeaks that emerge at the inner edges of the HBs, by using different real-frequency impurity solvers: perturbative methods [2], the density-matrix renormalization group (DMRG) [4–7], the numerical renormalization group (NRG) [8], and exact diagonalization [9, 10]. In contrast, quantum Monte Carlo solvers, which obtain the spectral functions on the real frequency axis via (numerically ill-posed) analytic continuation, have not found these subpeaks. The subpeaks give rise to distinct features in the momentum-resolved spectral function [5], measurable by photoemission spectroscopy [11, 12]. Despite these frequent consistent observations, the physical origin of the subpeaks and their relevance in more general (e.g., multi-flavor) models remained unclear.

In this work, we show that the subpeaks are induced by the effective doublon-holon (DH) [13] pair interaction originating from a second-order virtual process, where a doublon (holon) means an excitation that one particle is added to (removed from) a lattice site with average integer filling. We compute the correlation functions of doublon and holon operators in the SU(2) Hubbard model, by using DMFT with NRG [14, 15] as an impurity solver, and demonstrate that these correlation

functions manifest the peak structure associated with the subpeaks. We reproduce the peak structure of doublon and holon correlators via a mean-field analysis of the low-energy effective Hamiltonian obtained by a generalized Schrieffer-Wolff transformation (SWT) [16, 17]. Both approaches consistently result in a linear dependence of the subpeak position vs. interaction strength. From our DMFT+NRG calculations of general SU(N) Hubbard models for $N = 2, 3, 4$, we observe that the subpeaks become more pronounced with increasing N , since the DH pair excitations become more degenerate due to the larger SU(N) symmetry.

System.— The SU(N) Hubbard model describes N flavors of fermions on a lattice with local repulsive interactions, recently realized in ultracold atom experiments with tunable N [18]. The hopping amplitude v , the interaction strength U , and the chemical potential are flavor-independent, thus the system has SU(N) flavor symmetry. Its Hamiltonian is $H = H_U + H_v + H_\mu$, where $H_U = \frac{U}{2} \sum_i (\hat{n}_i - \bar{n})^2$, $H_v = v \sum_{\langle i,j \rangle, \nu} c_{i\nu}^\dagger c_{j\nu} + \text{h.c.}$, and $H_\mu = -\mu \sum_i \hat{n}_i$. Here $c_{i\nu}$ annihilates a particle of flavor $\nu = 1, \dots, N$ at lattice site i , $\hat{n}_i = \sum_\nu c_{i\nu}^\dagger c_{i\nu}$ is the particle number operator at site i , $\langle i, j \rangle$ indicates nearest neighbours, \bar{n} is a parameter for the desired average occupation, and μ is a fine tuning of chemical potential to achieve $\langle \hat{n}_i \rangle = \bar{n}$. Throughout this paper, we focus on $T = 0$ and the average occupation number as an integer closest to half filling $\bar{n} = \lfloor N/2 \rfloor$, by fixing $\mu = 0$ for $N = 2, 4$, and fine-tuning μ for $N = 3$.

Doublon and holon.— For integer average occupation \bar{n} , we define doublon and holon creation operators as

$$d_{i\nu}^\dagger \equiv P_{i, \bar{n}+1} c_{i\nu}^\dagger, \quad h_{i\nu}^\dagger \equiv P_{i, \bar{n}-1} c_{i\nu}, \quad (1)$$

where P_{in} means the projector onto the subspace in which the site i has n particles. For the SU(2) case, at half filling, $\bar{n} = 1$, these operators reduce to $d_{i\nu} = c_{i\nu} \hat{n}_{i\bar{\nu}}$, $h_{i\nu} = c_{i\nu}^\dagger (1 - \hat{n}_{i\bar{\nu}})$ with $\hat{n}_{i\nu} = c_{i\nu}^\dagger c_{i\nu}$ and $\bar{\nu} = 3 - \nu$, and they completely constitute the particle operator $c_{i\nu} = d_{i\nu} + h_{i\nu}^\dagger$. Then the particle correlator can be decomposed into four doublon and holon correlators, $A_{cc^\dagger}(\omega) = A_{dd^\dagger} + A_{dh} + A_{h^\dagger d^\dagger} + A_{h^\dagger h}$, where $A_{XY}(\omega) \equiv$

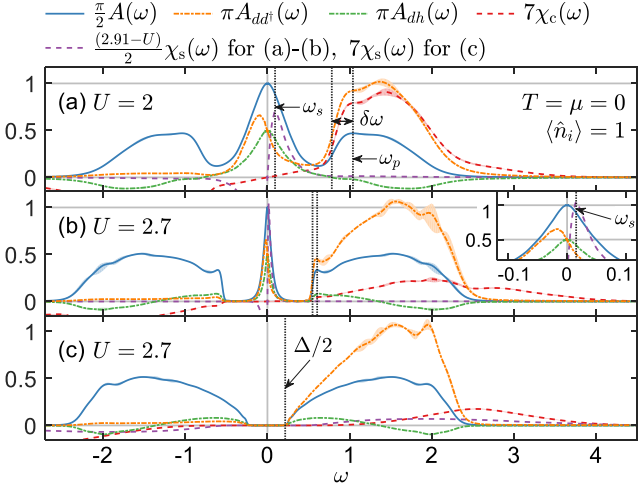


FIG. 1. Local correlation functions in (a)-(b) the metallic and (c) insulating phases of the SU(2) Hubbard model: the local spectral function $A(\omega)$ (blue solid lines), the correlators of doublon $d_{i\nu}$ and holon $h_{i\nu}$ operators [cf. Eq. (1)] (dash-dotted lines), charge susceptibility $\chi_c = A_{\delta\hat{n},\delta\hat{n}}$ (red dashed lines), and spin (i.e., flavor) susceptibility $\chi_s = A_{\vec{S},\vec{S}}/3$ (purple dashed lines), with $\chi_{c(s)}(\omega) = -\chi_{c(s)}(-\omega)$, $A_{dd^\dagger}(\omega) = A_{h^\dagger h}(-\omega)$, and $A_{dh}(\omega) = A_{h^\dagger d^\dagger}(\omega)$. Here $\delta\hat{n}_i \equiv \hat{n}_i - \langle \hat{n}_i \rangle$ and \vec{S}_i is the spin operator at site i . Each correlator is discretization-averaged (see Sec. I B of Ref. [19]) where the corresponding color-matched shaded area provides an estimate for numerical uncertainties, noticeable only in the HBs. Panels (b) and (c) show different solutions for the same value of U in the coexistence regime. In panel (b), inset zooms into the region of the QP. We mark the location of spectral features by vertical dotted lines: (a)-(b) subpeak position ω_p (defined as the local maximum near the inner HB edge), subpeak width $\delta\omega$ [defined as the minimum positive value satisfying $A(\omega_p - \delta\omega) = A(\omega_p)/2$], spin susceptibility peak position ω_s , and (c) inner HB edge at $\Delta/2$, where Δ is the Mott gap.

$\frac{-1}{\pi} \text{Im}G_{XY}(t)$, with $G_{XY}(t) = -i\vartheta(t)\langle [X(t), Y(0)]_\pm \rangle_T$ being the retarded correlation function of the fermionic (+) or bosonic (-) local operators X and Y acting on the same site. In the particle-hole symmetric case, only two correlators are independent: “diagonal” correlators $A_{dd^\dagger}(\omega) = A_{h^\dagger h}(-\omega)$ which are asymmetric, and “off-diagonal” correlators $A_{h^\dagger d^\dagger}(\omega) = A_{dh}(\omega)$ which are symmetric under $\omega \leftrightarrow -\omega$. For $N > 2$ flavors, the decomposition of $c_{i\nu}$ acquires more terms than $d_{i\nu}$ and $h_{i\nu}^\dagger$ [17].

DMFT+NRG.— We use single-site DMFT which maps the Hubbard model onto the single-impurity Anderson model (SIAM) which provides paramagnetic solutions, by construction. We employ the semi-circular density of states of the Bethe lattice with half-bandwidth D , together with units $D = \hbar = k_B = 1$, throughout. We solve the SIAM by the full-density-matrix NRG (fdm-NRG; [20]), exploiting $U(1)_{\text{charge}} \otimes \text{SU}(N)_{\text{flavor}}$ symmetry [21]. The coarse-grained discretization-averaged spectral data is broadened adaptively [19, 22] for best possible spectral resolution at higher energies, while preserving the intrinsic accuracy of NRG at low energies [e.g., the Luttinger pinning [23] $\frac{\pi}{2}A(\omega = 0) = 1$ in the metallic

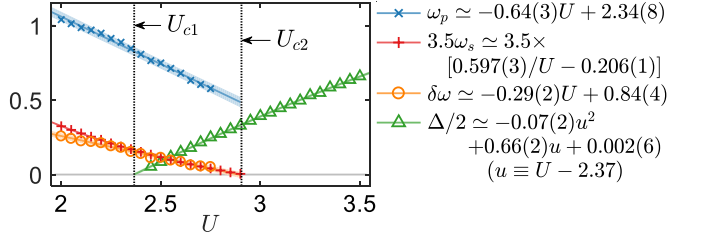


FIG. 2. The U -dependence of the spectral features: the position ω_p and width $\delta\omega$ of the subpeaks, the peak position ω_s of spin susceptibility χ_s and the Mott gap Δ (cf. Fig. 1). Symbols are data points from the DMFT+NRG calculations, lines are fits, and shading gives the 95% prediction bounds of fitting. The zeros of the extrapolated fits of Δ and ω_s yield estimates for the critical interaction strengths $U_{c1} = 2.37(2)$ and $U_{c2} = 2.91(1)$, respectively.

phase is accurately satisfied; see Fig. 1(a)-(b)].

SU(2) metallic phase.— We first consider the case $N = 2$ equivalent to the spin-full one-band Hubbard model. At $T = 0$ and half filling, a metallic phase exists for $U < U_{c2} = 2.91(1)$, and a paramagnetic insulating phase for $U > U_{c1} = 2.37(2)$. For $U_{c1} < U < U_{c2}$ the two phases coexist (e.g., see Fig. 2, or Refs. [3, 24]).

Within the metallic phase, the local spectral function $A(\omega)$ features one QP and two HBs [cf. Fig. 1(a)-(b)]. As U increases, the central QP narrows, the HBs widen, and the dips between the QP and the HBs deepen. On top of this, subpeaks are present at the inner edges of the HBs, whose position ω_p and width $\delta\omega$ decrease linearly with increasing U , as shown in Fig. 2.

Local spin (i.e., flavor) and charge susceptibilities, χ_s and χ_c [25], in Fig. 1 demonstrate that the QP and the HBs of $A(\omega)$ are tied to spin and charge degrees of freedom, respectively; that is, spin and charge excitations are energetically separated. The peak of χ_s indicates a spin-like collective mode responsible for the QP, which is analogous to the Kondo resonance in the SIAM in that the spin susceptibility peaks at the Kondo energy scale [26]. The position ω_s and width of the χ_s peak decrease as the QP narrows with increasing U ; especially, ω_s has a linear dependence vs. $1/U$, as shown in Fig. 2. In contrast, χ_c is suppressed within the QP region, while having long tails beyond the outer edges of the HBs.

For $T = 0^+$, the positive and negative energy sides of a correlator $A_{XY}(\omega)$ are derived from $\langle X(t)Y(0) \rangle_T$ and $\langle Y(0)X(t) \rangle_T = \langle X^\dagger(t)Y^\dagger(0) \rangle_T^*$, respectively. Therefore the upper HB in Fig. 1, which mainly consists of A_{dd^\dagger} , originates from the dynamics of the doublon $d_{i\nu}^\dagger(0)$. Another significant feature of A_{dd^\dagger} is a peak at $\omega = -\omega_s$. Just after the action of $d_{i\nu}(0)$ and just before $d_{i\nu}^\dagger(t)$, the site i has only spin- $\bar{\nu}$. Its time evolution between 0 and t with low frequency $|\omega| \simeq \omega_s$ is driven by the spin-like collective mode captured by the peak of χ_s at ω_s . In contrast, the off-diagonal correlator A_{dh} has a symmetric peak at $\omega = 0$. This reflects the particle-hole symmetric processes of destroying at the same site first a doublon and then a holon, or vice versa. A_{dd^\dagger} and A_{dh} contribute

comparably to the QP, having $A_{dd^\dagger}(0) = A_{dh}(0) = \frac{1}{2\pi}$.

In the metallic regime in Figs. 1(a)-(b) all of the doublon and holon correlators show peak-like features at $\omega = \pm\omega_p$. For $U \gtrsim 2.3$ [19], their contributions to these subpeaks have relative weights $A_{dd^\dagger}(\omega_p) > A_{dh}(\pm\omega_p) > A_{dd^\dagger}(-\omega_p)$. Our effective theory (described below) aims to reproduce this relative order of contributions, as well as the linear dependence of ω_p vs. U .

SU(2) insulating phase.— The QP, the subpeaks, the spin-charge separation in energy space, and the peaks of the doublon and holon correlators all disappear in the insulating phase, as depicted in Fig. 1(c). Instead, a Mott gap Δ opens, and χ_s and χ_c spread over a large energy range, $|\omega| > \Delta/2$, with suppressed heights. While both ω_p in the metallic phase and $\Delta/2$ in the insulating phase correlate to the location of the inner HB edges, their dependences on U are clearly different (see Fig. 2). Here the absence of subpeaks is consistent with previous studies [4–10]. Though other works [27–29] have reported subpeaks even in the insulating phase, their observations are not numerically stable due to, e.g., ill-posed analytic continuation or underbroadening.

DH pair interaction.— We will now demonstrate that the peaks of the doublon and holon correlators at $\omega = \pm\omega_p$, which add up to the subpeaks of $A(\omega)$, originate from a DH pair interaction within the low-energy effective Hamiltonian of the SU(2) Hubbard model. Our theory is based on the separation of three energy scales, $\omega_s < \omega_p < U/2$, corresponding to the QP, the subpeaks, and the HBs, respectively. We focus on the intermediate scale ω_p by integrating out the larger scale $U/2$ and by approximating the physics of the smaller scale ω_s .

We first integrate out the charge fluctuation of energy scale $U/2$, by employing a generalized SWT [16, 17]. We decompose the hopping term into different components $H_v = \sum_{m=-1}^{+1} H_{v;m}$ which cost Coulomb energy mU since $mUH_{v;m} = [H_U, H_{v;m}]$. Here $H_{v;0} \equiv v \sum_{\langle i,j \rangle, \nu} (d_{i\nu}^\dagger d_{j\nu} - h_{i\nu}^\dagger h_{j\nu}) + \text{h.c.}$ describes the hopping of doublons and holons without energy cost, whereas $H_{v;1} \equiv v \sum_{\langle i,j \rangle, \nu} (d_{i\nu}^\dagger h_{j\nu}^\dagger + d_{j\nu}^\dagger h_{i\nu}^\dagger)$ or $(H_{v;-1} = H_{v;1}^\dagger)$ creates (annihilates) nearest-neighbor DH pairs by paying (gaining) energy cost U . Then we write the low-energy effective Hamiltonian H_{eff} as a power series in v/U ,

$$H_{\text{eff}} = H_{v;0} + H_{ss} + H_{dh} + H_{3\text{-site}} + O(v^3/U^2), \quad (2)$$

$$H_{ss} = \frac{v^2}{U} \sum_{\langle i,j \rangle} 4\vec{S}_i \cdot \vec{S}_j - P_{i1}P_{j1},$$

$$\begin{aligned} H_{dh} &= \frac{2v^2}{U} \sum_{\langle i,j \rangle} (c_{j1}^\dagger c_{j2}^\dagger c_{i2} c_{i1} + P_{i2}P_{j0}) + (i \leftrightarrow j) \\ &= \frac{v^2}{U} \sum_{\langle i,j \rangle, \nu, \nu'} (h_{i\nu}^\dagger d_{j\nu}^\dagger + h_{j\nu}^\dagger d_{i\nu}^\dagger)(d_{i\nu'} h_{j\nu'} + d_{j\nu'} h_{i\nu'}), \end{aligned}$$

where $H_{3\text{-site}}$ is the sum of the products of operators at three nearest neighbor sites. The term $H_{ss} + H_{dh} + H_{3\text{-site}} = [H_{v;1}, H_{v;-1}]/U$, of order $O(v^2/U)$, can be interpreted as second-order virtual processes. H_{eff} is similar to the t - J model [30], widely used as the effective

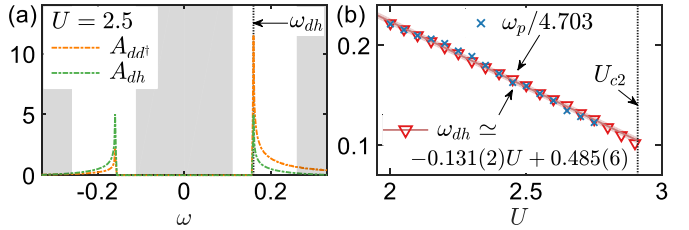


FIG. 3. (a) Doublon and holon correlators A_{dd^\dagger} (orange dash-dotted line) and A_{dh} (green dash-dotted line) from our effective theory for the metallic phase. Lower-energy spin dynamics at energies $|\omega| \lesssim \omega_s$ and higher energy scales $|\omega| \gtrsim U/2$ are neglected (as schematically indicated by the grey shading) by employing the generalized SWT together with a mean-field decoupling scheme. A_{dh} is symmetric, while A_{dd^\dagger} is asymmetric. Both lines have a pair of peaks at $\omega = \pm\omega_{dh}$, showing $A_{dd^\dagger}(\omega_{dh}) > A_{dh}(\pm\omega_{dh}) > A_{dd^\dagger}(-\omega_{dh})$. This is qualitatively consistent with the DMFT+NRG results for A_{dd^\dagger} and A_{dh} at $\omega = \pm\omega_p$ in Fig. 1(b) using the same color coding. (b) The peak position ω_{dh} from the effective theory decreases linearly with increasing U . The narrow shading gives the 95% prediction bounds of a linear fit. ω_{dh} nicely overlaps with ω_p (data taken from Fig. 2) up to an overall scaling factor. We take $\Delta_{dh} = 2.91 = U_{c2}$ independent of U , while the half-filled fraction $\langle P_{i1} \rangle$ is U -dependent, with the data taken from our DMFT+NRG results [19].

low-energy model for a Mott insulator, but additionally contains a three-site term, $H_{3\text{-site}}$, and, importantly, the DH term H_{dh} . Each term in Eq. (2) respects the $SU(2)_{\text{charge}} \otimes SU(2)_{\text{spin}}$ symmetry of the system. See Ref. [17] for a detailed derivation for general N . Hereafter we discard the higher order $O(v^3/U^2)$ terms.

The low-energy Hamiltonian H_{eff} in Eq. (2) describes two effective nearest-neighbor interactions whose role and relevance depend on the phase of the system: (i) H_{ss} contains the Heisenberg spin-spin interaction. In our paramagnetic metallic phase, this interaction induces a spin-like collective mode of energy scale ω_s . The interaction strength v^2/U is consistent with the scaling of $\omega_s \sim 1/U$ (cf. Fig. 2). On the other hand, H_{ss} becomes irrelevant in the paramagnetic insulating phase, where the spin susceptibility χ_s is overall suppressed. (ii) H_{dh} describes a DH pair interaction which is irrelevant in the insulating phase, since H_{dh} acts on the subspace with finite number of DH pairs, i.e., finite charge fluctuations. In the metallic phase, however, the density of DH pairs is finite.

Doublon and holon peaks.— After integrating out the largest energy scale U , we consider the doublon and holon dynamics governed by the effective Hamiltonian H_{eff} , aiming at the intermediate energy scale $\omega_p > \omega_s$, in the *metallic* phase. We simplify the physics at lower energies ($\lesssim \omega_s$) without exactly solving H_{eff} , by introducing two approximations described in detail in Ref. [17]: (i) We introduce a mean field, $\Delta_{dh} \equiv \frac{v}{2} \sum_\nu (d_{i\nu} h_{j\nu} + d_{j\nu} h_{i\nu})$, which regards the Fermi-liquid ground state as the “condensate” of the DH pairs. Then we approximate the DH interaction term as $H_{dh} \approx \frac{v}{U} \sum_{\langle i,j \rangle, \nu} \Delta_{dh}^* (d_{i\nu} h_{j\nu} + d_{j\nu} h_{i\nu}) + (\text{h.c.})$. The mean-field variable Δ_{dh} , comprised

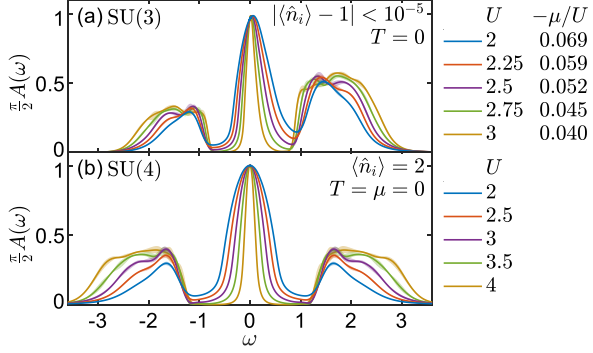


FIG. 4. Local spectral function $A(\omega)$ for (a) the SU(3) and (b) SU(4) Hubbard models in their metallic phases. Shading again reflects the uncertainties based on discretization-averaging (cf. Fig. 1). For $N = 3$, the chemical potential μ was fine-tuned to have the integer filling $\langle \hat{n}_i \rangle \simeq 1$ for different U , as shown in the legend of panel (a). For $N = 4$, we have $\mu = 0$ due to particle-hole symmetry. In all cases, being in the metallic regime, subpeaks emerge at the inner HB edges.

of the expectation value of the pair annihilation operator $d_{i\nu}h_{j\nu} + d_{j\nu}h_{i\nu}$, is reminiscent of Bardeen-Cooper-Schrieffer theory. Here the situation is quite different, though, in that charge conservation is actually not broken, given that the pair annihilation operator is nothing but a summand of the decomposed hopping term $H_{v,-1}$. The DH pairs are singlets of the $SU(2)^{\text{charge}} \otimes SU(2)^{\text{spin}}$ symmetry preserved in the metallic phase, and the mean-field approximation of H_{dh} also respects that symmetry [17]. (ii) We decouple the doublon and holon correlators from charge and spin density fluctuations. This is based on the numerical results that they are characterized by different energy scales: charge fluctuations are suppressed in the regime $|\omega| \lesssim U/2$, and spin fluctuations predominantly occur at energies $|\omega| \lesssim \omega_s$ (see Fig. 1). As a result, the equations of motion for the correlators close.

Fig. 3(a) shows the resulting doublon and holon correlators for finite Δ_{dh} in the metallic phase. They have a pair of peaks at $\omega = \pm\omega_{dh}$, akin to their peaks at $\omega = \pm\omega_p$ in Fig. 1. Fig. 3(b) demonstrates that the DH peak position ω_{dh} from the effective theory and the DMFT+NRG result of the subpeak position ω_p agree well up to overall scaling factor $\simeq 4.7$ which may be expected to arise given the crudeness of our approximations. In contrast, in the insulating phase H_{dh} is irrelevant, such that $\Delta_{dh} = 0$. As a consequence, the subpeaks are absent in the insulating phase.

Predictions for photoemission spectroscopy.— The QP and the HBs of the local spectral functions have already been observed in photoemission spectroscopy [11, 12]. This technique, which probes the momentum-resolved spectral function $A(\omega, \mathbf{k})$ (whose momentum average yields the local $A(\omega)$ discussed hitherto), should also be able to reveal the DH subpeaks. We have thus computed $A(\omega, \mathbf{k})$, see Figs. S3 and S4 of Ref. [19]. Our

$T = 0$ results agree with prior DMFT+DMRG results from Ref. [5], showing that the feature in $A(\omega, \mathbf{k})$, which leads to the subpeak in $A(\omega)$, has distinct dispersion, consistent with the interpretation of DH pair propagation. Going beyond Ref. [5], we also analyze finite T , and find that the subpeak-related features survive below the critical temperature for the Mott transition [19]. The distinct dispersion and T -dependence of the subpeak, correlated with those of the QP, distinguish it from other fine structure of the HBs originating from atomic levels. Thus we expect them to be observable, especially in multi-band materials where the subpeaks become more pronounced, as we discuss below.

SU($N > 2$) models.— We also analyze the SU(3) and SU(4) Hubbard models at integer filling $\langle \hat{n}_i \rangle = \lfloor N/2 \rfloor$, with the results shown in Fig. 4. Similar to the case $N = 2$ in Fig. 1, we again observe subpeaks on the inner edges of the HBs. While the subpeaks carry small weights compared with the rest of the HBs for $N = 2$ [cf. Fig. 1(b)], the subpeaks for $N = 3, 4$ have significantly larger relative weights (cf. purple lines in Fig. 4). Even for $N = 4$, the subpeaks are clearly higher than the rest of the HBs. Note that the QP persists more strongly at large $U \gtrsim 3$ for larger N , similarly to the widening of the Kondo peak in the SU(N) Kondo model [31].

We interpret this enhancement of the subpeaks, as resulting from the enlarged space of DH pair excitations in the SU($N > 2$) Hubbard models. Generalizing the DH interaction H_{dh} discussed above to the SU($N > 2$) cases, we find that the DH pair excitations on nearest neighbours are 3- and 15-fold degenerate in the SU(3) and SU(4) models, respectively, in contrast to the non-degeneracy in the SU(2) case [17]. A particularly promising area for studying this behaviour is ultracold atom physics, where pronounced DH correlations have been reported in the 2D Hubbard model [32].

Conclusion.— We showed that the subpeaks at the inner HB edges can be related to the effective DH pair interaction by using a generalized SWT. By using NRG as a real-frequency impurity solver for DMFT, we uncovered detailed dynamical information on the decomposition of the local spectral function into doublon and holon correlators. By utilizing a recently developed broadening scheme [22], we efficiently resolved those spectral features at high energies which had been considered challenging for the NRG in the past due to its logarithmic coarse graining. An effective theory based on the scale separation of the characteristic energy scales ω_s , ω_p , and U reproduces the linear U dependence of ω_p found numerically in DMFT+NRG. Our predictions should be testable using photoemission spectroscopy of correlated materials, or in ultracold atom systems.

We thank M. Bukov, G. Kotliar, A. Mitchell, K. Penc, A. Polkovnikov, M. Punk, and R. Žitko for fruitful discussion. This work was supported by Nanosystems Initiative Munich. S.L. acknowledges support from the Alexander von Humboldt Foundation and the Carl Friedrich von Siemens Foundation. A.W. from DFG WE4819/2-1.

[1] A. Georges, G. Kotliar, W. Krauth, and M. J. Rozenberg, Rev. Mod. Phys. **68**, 13 (1996); G. Kotliar, S. Y. Savrasov, K. Haule, V. S. Oudovenko, O. Parcollet, and C. A. Marianetti, Rev. Mod. Phys. **78**, 865 (2006).

[2] X. Y. Zhang, M. J. Rozenberg, and G. Kotliar, Phys. Rev. Lett. **70**, 1666 (1993).

[3] R. Bulla, Phys. Rev. Lett. **83**, 136 (1999).

[4] M. Karski, C. Raas, and G. S. Uhrig, Phys. Rev. B **72**, 113110 (2005).

[5] M. Karski, C. Raas, and G. S. Uhrig, Phys. Rev. B **77**, 075116 (2008).

[6] M. Ganahl, P. Thunström, F. Verstraete, K. Held, and H. G. Evertz, Phys. Rev. B **90**, 045144 (2014); M. Ganahl, M. Aichhorn, H. G. Evertz, P. Thunström, K. Held, and F. Verstraete, Phys. Rev. B **92**, 155132 (2015).

[7] F. A. Wolf, I. P. McCulloch, O. Parcollet, and U. Schollwöck, Phys. Rev. B **90**, 115124 (2014).

[8] R. Žitko and T. Pruschke, Phys. Rev. B **79**, 085106 (2009).

[9] M. Granath and H. U. R. Strand, Phys. Rev. B **86**, 115111 (2012).

[10] Y. Lu, M. Höppner, O. Gunnarsson, and M. W. Haverkort, Phys. Rev. B **90**, 085102 (2014).

[11] S.-K. Mo, J. D. Denlinger, H.-D. Kim, J.-H. Park, J. W. Allen, A. Sekiyama, A. Yamasaki, K. Kadono, S. Suga, Y. Saitoh, T. Muro, P. Metcalf, G. Keller, K. Held, V. Evertz, V. I. Anisimov, and D. Vollhardt, Phys. Rev. Lett. **90**, 186403 (2003).

[12] A. Sekiyama, H. Fujiwara, S. Imada, S. Suga, H. Eisaki, S. I. Uchida, K. Takegahara, H. Harima, Y. Saitoh, I. A. Nekrasov, G. Keller, D. E. Kondakov, A. V. Kozhevnikov, T. Pruschke, K. Held, D. Vollhardt, and V. I. Anisimov, Phys. Rev. Lett. **93**, 156402 (2004).

[13] H. Yokoyama, M. Ogata, and Y. Tanaka, J. Phys. Soc. Jpn. **75**, 114706 (2006); P. Phillips, Rev. Mod. Phys. **82**, 1719 (2010); T. Sato and H. Tsunetsugu, Phys. Rev. B **90**, 115114 (2014); S. Zhou, Y. Wang, and Z. Wang, Phys. Rev. B **89**, 195119 (2014); P. Prelovšek, J. Kokalj, Z. Lenarčič, and R. H. McKenzie, Phys. Rev. B **92**, 235155 (2015); S. Zhou, L. Liang, and Z. Wang, arXiv:1605.03597.

[14] K. G. Wilson, Rev. Mod. Phys. **47**, 773 (1975).

[15] R. Bulla, T. A. Costi, and T. Pruschke, Rev. Mod. Phys. **80**, 395 (2008).

[16] M. Bukov, M. Kolodrubetz, and A. Polkovnikov, Phys. Rev. Lett. **116**, 125301 (2016); M. Bukov, L. D'Alessio, and A. Polkovnikov, Adv. Phys. **64**, 139 (2015).

[17] S.-S. B. Lee, J. von Delft, and A. Weichselbaum, Submitted to Phys. Rev. B.

[18] S. Taie, R. Yamazaki, S. Sugawa, and Y. Takahashi, Nat. Phys. **8**, 825 (2012); C. Hofrichter, L. Rieger, F. Scazza, M. Höfer, D. R. Fernandes, I. Bloch, and S. Fölling, Phys. Rev. X **6**, 021030 (2016).

[19] See Supplementary Material, which contains Refs. [33–35], for additional numerical results and technical details.

[20] A. Weichselbaum and J. von Delft, Phys. Rev. Lett. **99**, 076402 (2007); A. Weichselbaum, Phys. Rev. B **86**, 245124 (2012).

[21] A. Weichselbaum, Ann. Phys. **327**, 2972 (2012).

[22] S.-S. B. Lee and A. Weichselbaum, Phys. Rev. B **94**, 235127 (2016).

[23] E. Müller-Hartmann, Z. Phys. B **76**, 211 (1989).

[24] R. Bulla, T. A. Costi, and D. Vollhardt, Phys. Rev. B **64**, 045103 (2001).

[25] C. Raas and G. S. Uhrig, Phys. Rev. B **79**, 115136 (2009).

[26] M. Hanl and A. Weichselbaum, Phys. Rev. B **89**, 075130 (2014).

[27] S. Nishimoto, F. Gebhard, and E. Jeckelmann, J. Phys.: Condens. Matter **16**, 7063 (2004).

[28] E. Gull, D. R. Reichman, and A. J. Millis, Phys. Rev. B **82**, 075109 (2010).

[29] M. Granath and J. Schött, Phys. Rev. B **90**, 235129 (2014).

[30] A. B. Harris and R. V. Lange, Phys. Rev. **157**, 295 (1967); K. A. Chao, J. Spalek, and A. M. Oles, J. Phys. C **10**, L271 (1977); A. H. MacDonald, S. M. Girvin, and D. Yoshioka, Phys. Rev. B **37**, 9753 (1988); H. Eskes and A. M. Oleś, Phys. Rev. Lett. **73**, 1279 (1994); H. Eskes, A. M. Oleś, M. B. J. Meinders, and W. Stephan, Phys. Rev. B **50**, 17980 (1994); A. L. Chernyshev, D. Galanakis, P. Phillips, A. V. Rozhkov, and A.-M. S. Tremblay, Phys. Rev. B **70**, 235111 (2004).

[31] A. C. Hewson, *The Kondo Problem to Heavy Fermions* (Cambridge University Press, 1993).

[32] L. W. Cheuk, M. A. Nichols, K. R. Lawrence, M. Okan, H. Zhang, E. Khatami, N. Trivedi, T. Paiva, M. Rigol, and M. W. Zwierlein, Science **353**, 1260 (2016).

[33] F. B. Anders and A. Schiller, Phys. Rev. Lett. **95**, 196801 (2005); Phys. Rev. B **74**, 245113 (2006).

[34] R. Bulla, A. C. Hewson, and T. Pruschke, J. Phys.: Condens. Matter **10**, 8365 (1998).

[35] K. Byczuk, M. Kollar, K. Held, Y. F. Yang, I. A. Nekrasov, T. Pruschke, and D. Vollhardt, Nat. Phys. **3**, 168 (2007); C. Raas, P. Grete, and G. S. Uhrig, Phys. Rev. Lett. **102**, 076406 (2009).

Supplementary Material

Here we discuss the technical details of the calculations in the main text together with supplementary results. In Sec. I, we explain the algorithm and parameters in our NRG calculations. In Sec. II, we provide DMFT+NRG results supplementing the analysis in the main text.

The equations and figures in the Supplementary Material are referred to as numbers with S (e.g., Fig. S1), while those in the main text are referred to as numbers without S (e.g., Fig. 1). Also the citations occurring in the Supplementary Material refer to references given in the main text.

I. METHODS

We first summarize the procedure of the full-density-matrix NRG (fdm-NRG; [20]). Then we explain two techniques utilized in this work: adaptive broadening [22] for improving spectral resolution and Λ -averaging for suppressing discretization artifact. We also emphasize some technical aspects concerning the application of NRG to the DMFT.

A. Full-density-matrix NRG

We consider a single-impurity Anderson model (SIAM) in which the hybridization function between the impurity and the bath is given by $\Gamma^{\text{in}}(\omega)$. The bath of the SIAM is discretized in energy space with logarithmic energy grid $\pm\omega_{\text{max}}\Lambda^{-k-z}$, where $\Lambda > 1$ is the NRG discretization parameter, $k \in \mathbb{N}_0$ the grid index, and $z \in [0, 1]$ the discretization shift (“ z -shift”) with integer n_z . The prefactor ω_{max} specifies the maximum non-zero range of the input $\Gamma^{\text{in}}(\omega)$; see Sec. I D for its determination. The value of z is fixed for each separate NRG calculation. The representative energy of each discretization interval is determined by solving a differential equation [8].

The discretized impurity-bath Hamiltonian is tridiagonalized to yield a semi-infinite tight-binding chain, so-called Wilson chain. The logarithmic discretization results in an overall exponential decay of the hopping amplitudes and the on-site energies in the chain. Note that the on-site energies vanish for particle-hole symmetric cases $\Gamma^{\text{in}}(\omega) = \Gamma^{\text{in}}(-\omega)$. In virtue of this exponential decay, energy scale separation ensures that the complete set of (well approximated) energy eigenvalues $\{E_i^z\}$ and eigenstates $\{|E_i^z\rangle\}$ of the Wilson chain can be constructed via the iterative diagonalization [33], where the superscript z indicates the dependence on z -shift.

Using the complete basis of energy eigenstates, we can compute the discrete spectrum $A_{\text{disc}}^z(\omega)$ of general correlation function $A_{O_1, O_2}(\omega)$ in the Lehmann representation [20],

$$A_{\text{disc}}^z(\omega) = \sum_{ij} A_{ij}^z \delta(\omega - \omega_{ij}^z), \quad (\text{S1a})$$

$$A_{ij}^z \equiv \langle E_i^z | O_1 | E_j^z \rangle \langle E_j^z | O_2 | E_i^z \rangle (\rho_i^z \pm \rho_j^z), \quad (\text{S1b})$$

$$\omega_{ij}^z \equiv E_j^z - E_i^z, \quad (\text{S1c})$$

where $\rho_i^z = e^{-E_i^z/T} / \sum_{i'} e^{-E_{i'}^z/T}$ is the diagonal element of the density matrix at temperature T , \pm in Eq. (S1b) takes the value $-(+)$ for (anti-)commuting operators O_1 and O_2 , and we set $k_B = \hbar = 1$. The ω_{ij}^z values that determine the positions of the δ functions in A_{disc}^z are bunched, and the bunches occur roughly at $\omega \sim \pm\Lambda^{-k-z}$ ($k \in \mathbb{Z}$), reflecting the logarithmic discretization of the system [22]. To reduce discretization artefacts, we average over different choices of z and Λ , as described in more detail in Sec. I B below.

The computational efficiency and accuracy in the iterative diagonalization and in computing A_{disc}^z can be largely enhanced, especially for multi-band problems, by exploiting non-Abelian symmetries [21]. In this work we obtain the energy eigenstates as the multiplets of $U(1)_{\text{charge}} \otimes SU(N)_{\text{flavor}}$ symmetry. In the iterative diagonalization, we keep up to $N_{\text{keep}} = 3000$ multiplets at each step. After the first $\lceil 2 \log_{\Lambda} 100 \rceil$ iterations, we discard the multiplets with rescaled energy above $E_{\text{trunc}} = 9$ for efficiency [20].

B. Discretization averaging

A drawback of the logarithmic discretization is that the *input* hybridization function, $\Gamma^{\text{in}}(\omega)$, is poorly resolved at high energies; for example, each Hubbard band in Fig. 1 contains only two or three discretization intervals. This is not a problem when Γ^{in} is featureless (as in usual impurity problems) or when the correlation functions are overbroadened at high energies (as in previous DMFT+NRG calculations), but it can induce some artificial features in correlation functions when Γ^{in} has structure and the correlation functions are finely resolved (as in our current DMFT+NRG calculations). Since not only physical structure but also artifacts (e.g., unphysical wriggle, overbroadening) can be self-reinforced during the self-consistency loop, it is necessary to suppress such discretization artifacts.

We address this problem by averaging over several discretization settings using a combination of two different schemes. The first, called *z-averaging*, is standard practice in NRG [8, 15]: one averages spectral functions computed for a fixed value of Λ over n_z equally distributed z -shifts $z \in \{1/n_z, 2/n_z, \dots, 1\}$. The resulting discrete energy grids all have the same spacing on a logarithmic energy scale, but are shifted relative to each other. This *z*-averaging is also used to improve the spectral resolution of correlation functions (see Sec. I C below for detail). In addition, we use a second averaging scheme, which we refer to as *Λ -averaging*, which involves an average over different coarse grainings on the logarithmic energy scale.

We implemented these two schemes in the following manner. We first obtain multiple curves for the same correlation function by independent NRG runs using sets of

different z and Λ values. After z -averaging the discrete data for the same Λ followed by broadening, we then average these curves over Λ . The Λ -averaged curve of hybridization function is fed back into the DMFT self-consistency loop (see Sec. I D below for detail). With only two or three different Λ 's, the discretization artifacts can be significantly suppressed. In this work, we average over curves computed using the following combinations: $(\Lambda, n_z, \alpha) = (1.7, 6, 1.47), (2, 8, 1.5), (2.3, 10, 1.56)$ for the SU(2) case in Fig. 1, and $(\Lambda, n_z, \alpha) = (2.6, 8, 1.451), (3.2, 10, 1.49), (4, 12, 1.5)$ for the SU($N > 2$) case in Fig. 4. Here α is a parameter for broadening correlation functions (see Sec. I C below), and the tuples (Λ, n_z, α) are chosen to have comparable ratios of $\frac{\alpha}{n_z} \ln \Lambda$ for each case. This Λ -averaging can be used to estimate error bars for discretization related artifacts: the shadings in Figs. 1, 4, and S1 depict the lower and upper bounds of the curves of different Λ 's, while the lines show the Λ -averaged curves.

C. Adaptive broadening

Physically, A_{O_1, O_2} should be a continuous function of ω , since the original impurity model features a continuous bath before the discretization. For $T = 0$, we broaden $A_{\text{disc}}^z(\omega)$ by replacing δ functions with the log-Gaussian kernels,

$$\delta(\omega - \omega') \Rightarrow \tilde{\delta}_\sigma(\omega; \omega') \equiv \frac{\Theta(\omega\omega')}{\sqrt{\pi}\sigma|\omega'|} e^{-\left(\frac{\ln|\omega/\omega'|}{\sigma} - \frac{\sigma}{4}\right)^2}, \quad (\text{S2})$$

where σ is a broadening width in log-frequency scale. For $T \neq 0$, the broadening kernels are modified from Eq. (S2), see Ref. [22] for details. Based on the observation on the bunching of δ functions roughly at $\omega \sim \Lambda^{-k-z}$, the conventional broadening scheme uses constant σ for all spectral contributions, i.e., the broadening width for a weight A_{ij}^z in linear-frequency scale is simply proportional to $|\omega_{ij}^z|$. Thus the spectral features at high energies (e.g., side peaks) are generally overbroadened by the conventional scheme; the bunches contributing to such features are distributed in an “irregular” manner that does not follow the Λ^{-k-z} pattern.

A recipe to improve the spectral resolution within the conventional broadening scheme is z -averaging (see also above), where one broadens the discrete data averaged over different NRG calculations of A_{disc}^z for different z -shifts, $\bar{A}(\omega) = \frac{1}{n_z} \sum_z A_{\text{disc}}^z(\omega)$. Since the δ -function bunches at $\omega \sim \Lambda^{-k-z}$ for a given z -shift interlace with the bunches for the other z -shifts, one can use a narrower width, $\sigma \propto 1/n_z$, to achieve the continuity. Then the resolution improves as n_z increases, but the improvement is limited [22].

Recently, two of the authors developed an adaptive broadening scheme [22] which further enhances the spectral resolution at high energies, in combination with z -averaging. The adaptive scheme broadens each discrete

peak in $\bar{A}(\omega)$ with individual width: $\delta(\omega - \omega_{ij}^z)$ is broadened to $\tilde{\delta}_{\sigma_{ij}}(\omega; \omega_{ij}^z)$, where

$$\sigma_{ij} = \frac{\alpha}{n_z} \frac{d \ln |\omega_{ij}^z|}{dz} = \frac{\alpha}{n_z |\omega_{ij}^z|} \left| \frac{dE_j^z}{dz} - \frac{dE_i^z}{dz} \right|, \quad (\text{S3})$$

and α is overall prefactor of order $O(1)$. Here σ_{ij}/α estimates the distance on log-frequency scale, from one bunch of δ functions at ω_{ij}^z for a given z -shift to its neighbouring bunch at $\omega_{ij}^{z+(1/n_z)}$ for the next z -shift; this estimate captures the irregular distribution of δ -function bunches contributing to the spectral features at high energies, and assigns smaller broadening widths σ_{ij} for these bunches.

As a result, the adaptive scheme better resolves such features, and the enhancement is more significant for larger Λ or smaller n_z . Of course, the adaptive scheme retains the intrinsic accuracy of NRG at low energies; the Friedel sum rule and the Luttinger pinning are fulfilled with sub-1% error. Note that, in this work, we use the lower bound $\sigma_{ij} \geq (\ln \Lambda)/15$ to avoid unnecessary under-broadening.

D. DMFT

We use single-site DMFT based on the semi-circular density of states $\rho_0(\omega) = \frac{2}{\pi D^2} \sqrt{D^2 - \omega^2}$ for the non-interacting lattice, corresponding to a Bethe lattice of coordination number $z \rightarrow \infty$ and $v \propto 1/\sqrt{z}$. We set the half-bandwidth $D \equiv 2v\sqrt{z} := 1$ as the unit of energy, as well as $\hbar = 1$ throughout.

In the coexistence region of the metallic and insulating phases (for $U_{c1} < U < U_{c2}$ in our Hubbard models at $T = 0$), the metallic (insulating) choice of Γ^{in} as the initial seed in the self-consistency loop results in a metallic (insulating) solution. As the metallic and insulating initial seeds, we chose the metallic solution $\pi D^2 \rho_0(\omega)/4 = \sqrt{D^2 - \omega^2}/2$ (which is the exact solution for $U = 0$), and the insulating solution for $U = 3.2D$ (obtained by using the $U = 0$ solution as the initial seed), respectively.

In each iteration (except for the first iteration), $\Gamma^{\text{in}}(\omega)$ is determined by the result from the previous iteration that has exponentially decaying tails at large frequencies; we define ω_{max} as the largest energy satisfying $\Gamma^{\text{in}}(\omega_{\text{max}}) = \max(\Gamma^{\text{in}})/100$, without loss of generality. Then we define the discretization grid $\pm \omega_{\text{max}} \Lambda^{-k-z}$ as mentioned above. We compute the impurity self-energy as the ratio of two correlation functions, $\Sigma_{\text{imp}} \equiv \langle [c_{\text{imp},\nu}, \frac{U}{2} n_{\text{imp}}(n_{\text{imp}} - 1)] | | c_{\text{imp},\nu}^\dagger \rangle_\omega / \langle c_{\text{imp},\nu} | | c_{\text{imp},\nu}^\dagger \rangle_\omega$ [34], where $\langle X | | Y \rangle_\omega = G_{XY}(\omega)$ is the retarded correlation function, $c_{\text{imp},\nu}$ annihilates a particle of flavor ν at the impurity, and $n_{\text{imp}} = \sum_\nu c_{\text{imp},\nu}^\dagger c_{\text{imp},\nu}$.

As we consider the semi-elliptic density of states $\rho_0(\omega)$ of the lattice, the local spectral function $A(\omega)$ and the hybridization function $\Gamma^{\text{out}}(\omega) = \pi D^2 A(\omega)/4$ for the next

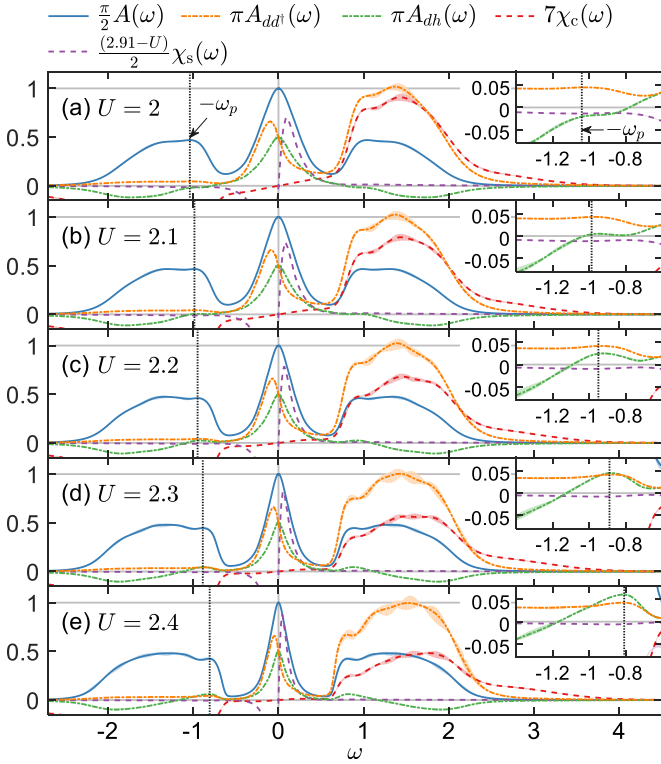


FIG. S1. Local correlation functions for $2 \leq U \leq 2.4$ in the SU(2) model. Refer to the caption of Fig. 1 in the main text for the description of lines and shades. Insets zoom into the region $\omega \sim -\omega_p, -U/2$, and the vertical dotted line indicates the location of the left subpeak $-\omega_p$.

iteration can be derived from Σ_{imp} via an explicit relation $A(\omega) = \frac{-2}{\pi D^2} \text{Im}(\xi - \sqrt{\xi^2 - D^2})$ without numerical integration, where $\xi \equiv \omega + \mu - \Sigma_{\text{imp}}$. We continue the loop until the self-consistency criterion $|\Gamma^{\text{in}} - \Gamma^{\text{out}}| < \pi/10^3$ is satisfied.

The above relation between Σ_{imp} and $A(\omega)$, which originates from the semi-ellipticity of ρ_0 , leads to two interesting properties at self-consistency, when $\Gamma^{\text{in}} = \Gamma^{\text{out}}$: (i) the impurity Green's function $(\xi - \Gamma^{\text{in}})^{-1}$, improved by using self-energy [34], is equivalent to the local lattice Green's function $\frac{2}{D^2}(\xi - \sqrt{\xi^2 - D^2})^{-1}$. (ii) Since $\Sigma_{\text{imp}} = \omega + \mu - (\langle c_{\text{imp},\nu} | |c_{\text{imp},\nu}^\dagger \rangle_\omega)^{-1} - \frac{D^2}{4} \langle c_{\text{imp},\nu} | |c_{\text{imp},\nu}^\dagger \rangle_\omega$, the kinks (i.e., big changes in the first derivatives) of Σ_{imp} [35] and $A_{cc^\dagger} \equiv \frac{-1}{\pi} \text{Im} \langle c_{i\nu} | |c_{i\nu}^\dagger \rangle_\omega$ are directly related. Therefore, the sharp peaks of $A_{dd^\dagger}(-\omega_s)$ and $A_{h^\dagger h}(\omega_s)$ [cf. Fig. 1] result in the kinks in A_{cc^\dagger} as well as those in Σ_{imp} .

II. SUPPLEMENTARY RESULTS

Fig. S1 shows how the correlation functions in the metallic phase change for $2 \leq U \leq 2.4$. This is similar to Fig. 1, except for the narrower range in U and the zooms into $\omega \sim -\omega_p$ in the insets. The peak of the

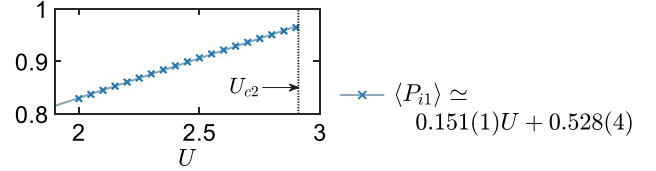


FIG. S2. Probability of single occupation $\langle P_{i1} \rangle$ vs U of the SU(2) Hubbard model. Symbols are data points from the DMFT+NRG calculations and line is fit. The 95% prediction bounds of fitting is invisibly narrow.

off-diagonal correlators, $A_{dh}(\pm\omega_p)$ or $A_{h^\dagger d^\dagger}(\pm\omega_p)$, grows with increasing U ; while it is only a shoulder for $U \lesssim 2$, for $U \gtrsim 2.3$ it becomes a peak that actually exceeds the shallow peak of the diagonal correlators, $A_{dd^\dagger}(-\omega_p)$ or $A_{h^\dagger h}(\omega_p)$. Note that the off-diagonal correlators are negative for $|\omega| \gtrsim U/2$ for $U \gtrsim 2.1$ and their full integrals are zero by sum rule. In contrast, the diagonal correlators are positive, throughout, by construction.

Fig. S2 shows the data for the probability of single occupation $\langle P_{i1} \rangle$ which entered the mean-field decoupling analysis in Fig. 3 in the main text. It shows a clear linear dependence on U .

Up to now, we have shown the local (i.e., momentum-averaged) correlation functions at $T = 0$. In photoemission spectroscopy experiments, the spectral functions are usually measured resolved in momentum \mathbf{k} at finite T . Therefore we have also studied the momentum-resolved spectral functions,

$$A(\omega, \epsilon_{\mathbf{k}}) = \frac{-1}{\pi} \text{Im} \frac{1}{\omega + \mu - \epsilon_{\mathbf{k}} - \Sigma(\omega) + i0^+},$$

with the results presented in Figs. S3 and S4 for the half-filled SU(2) Hubbard model for different values of U and T . In the DMFT, since the self-energy Σ is approximated to be independent of \mathbf{k} , the \mathbf{k} -dependence of the spectral function appears only as the dependence on the non-interacting single-particle energy $\epsilon_{\mathbf{k}}$ with momentum \mathbf{k} , i.e., $A(\omega, \mathbf{k}) = A(\omega, \epsilon_{\mathbf{k}})$. For comparison, we also plot the local spectral function $A(\omega)$, which is the average of $A(\omega, \epsilon_{\mathbf{k}})$ over momentum space,

$$A(\omega) = \int d\epsilon \rho_0(\epsilon) A(\omega, \epsilon),$$

where $\rho_0(\epsilon) = \frac{2}{\pi D^2} \sqrt{D^2 - \epsilon^2}$ is the density of states for non-interacting lattice considered for our DMFT calculations. Here we plot only the spectral functions for negative frequencies, since the photoemission spectroscopy mainly accesses the energy below the Fermi level. At half filling, one has for positive frequencies by particle-hole symmetry: $A(\omega) = A(-\omega)$ and $A(\omega, \epsilon_{\mathbf{k}}) = A(-\omega, -\epsilon_{\mathbf{k}})$.

Fig. S3 illustrates how $A(\omega, \epsilon_{\mathbf{k}})$ evolves with increasing U . For the metallic results in panels (a)-(c), there are two most pronounced ridges of spectral intensity: First, one ridge extends from the origin at $(\omega, \epsilon_{\mathbf{k}}) = (0, 0)$. By parametrizing its ridge line as $\omega_0(\epsilon_{\mathbf{k}})$, we find an

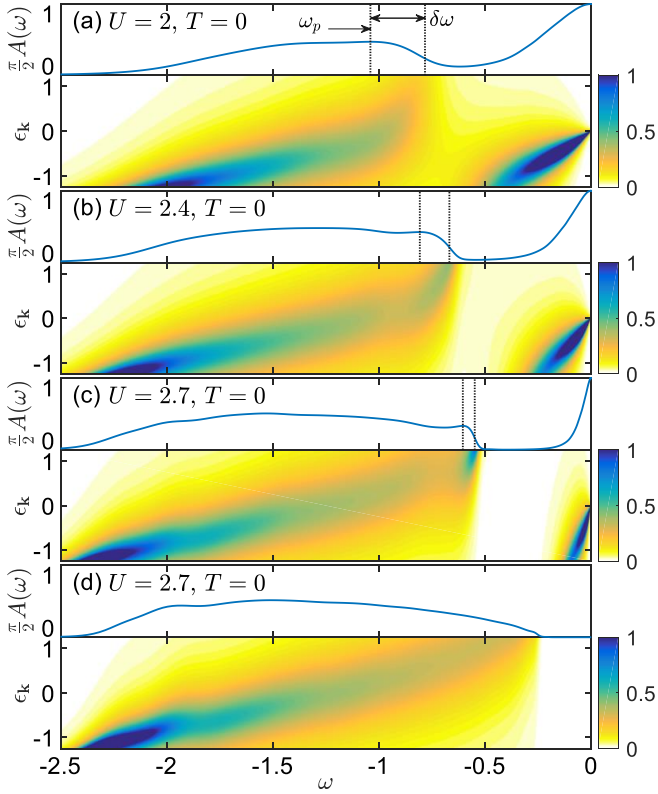


FIG. S3. Local spectral function $A(\omega)$ (upper line plots) and momentum-resolved spectral function $A(\omega, \epsilon_k)$ (lower color plots) in (a)-(c) the metallic and (d) insulating phases of the half-filled SU(2) Hubbard model, for different values of U at $T = 0$. For panels (a)-(c) we initiated the DMFT loop with metallic local spectral function, while for panel (d) with an insulating one; see Sec. ID for detail. Hence panels (c) and (d) lie in the coexistence regime, which exhibits two different phases for the same value of $U = 2.7$. The range, i.e., position and width, of the subpeak in panels (a)-(c) are indicated by vertical dotted lines.

approximately linear dispersion, $\omega_0 \simeq Z\epsilon_k$. The slope $Z = m_0/m^*$ corresponds to the inverse effective mass of the quasiparticle [equivalently, Z is the quasiparticle weight proportional to the peak position ω_s of the local spin susceptibility, i.e., $Z \approx 3\omega_s$]. As U increases, the effective mass m^* diverges at $U = U_{c2}$. Therefore the slope $d\omega_0/d\epsilon_k$ goes to zero, as the QP disappears entirely. Second, a broad ridge is associated with the lower HB in $A(\omega)$ which stretches over a wide range of energies $\omega \lesssim -D$.

In Fig. S3(b)-(c), another intermediate ridge, whose ridge line is parametrized as $\omega_1(\epsilon_k)$, appears in the region $\omega_1 \simeq -\omega_p$ and $\epsilon_k \lesssim 1$, which contributes to a subpeak in $A(\omega)$ at $\omega = -\omega_p$. As U increases within the metallic phase, this ridge becomes more pronounced, sharper, and better separated from the other ridges. On the other hand, in the insulating phase as in panel (d), both, the ridges for the subpeak and quasiparticle, disappear. Therefore the occurrence or not of this intermediate

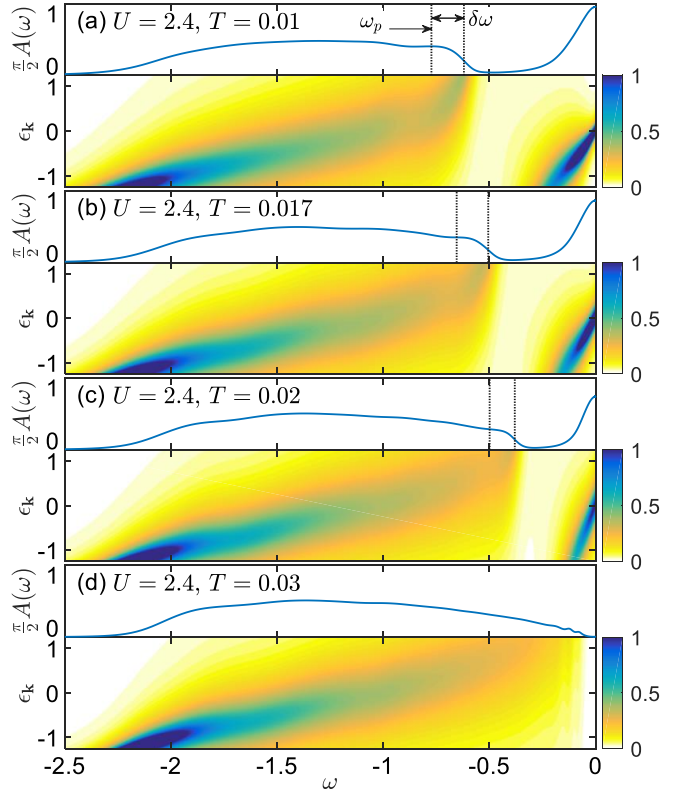


FIG. S4. Similar analysis as in Fig. S3, but for constant $U = 2.4$ while changing T . For all panels, we initiated the DMFT loop with metallic local spectral function; see Sec. ID for detail.

ridge is completely tied to the behavior already seen in the spectral function $A(\omega)$ itself.

Note that this result is consistent with the DMFT+DMRG calculation for $T = 0$ by Karski *et al.* [5]. Compared to the DMFT+DMRG results of Ref. [5], the spectral resolution achieved here by DMFT+NRG is better at low energies and similar at high energies. While the former is to be expected, the latter is not, due to the reliance of NRG on logarithmic discretization. Here we nevertheless achieve a rather high resolution even at high energies by using the refined broadening scheme developed in Ref. [22].

The range of the dispersion of the intermediate ridge is comparable with the subpeak width $\delta\omega$ in $A(\omega)$. It is also consistent with the result in Fig. 2 where $\delta\omega \approx 3.5\omega_s$ for large $U > 2.5$. The slope $d\omega_1/d\epsilon_k$ for larger ϵ_k on the order of the half-bandwidth $D = 1$ is roughly half of the quasiparticle weight $Z \simeq d\omega_0/d\epsilon_k$, which suggests that the underlying object responsible for the subpeaks has about twice the effective mass of an individual quasiparticle. In this sense our NRG-based numerical results are consistent with our interpretation of the subpeaks as arising from doublon-hole pairs.

The temperature dependence of the momentum-resolved spectral function $A(\omega, \epsilon_k)$ is analyzed in Fig. S4. As T increases, the subpeak in $A(\omega)$ and the subpeak

ridge in $A(\omega, \epsilon_{\mathbf{k}})$ become suppressed and blurred, in accordance with the suppression of the quasiparticle-related spectral features. This is consistent with our effective theory that the subpeaks originate from the doublon and holon excitations on top of the Fermi-liquid ground state,

which serves as as the DH condensate. When the Fermi-liquid quasiparticles become ill-defined, also the DH condensate breaks down. Despite such thermal suppression, we emphasize that the subpeak-related features are still visible at temperatures as large as $T \lesssim 0.02$, i.e., close to the critical temperature is $T_c(U = 2.4) \simeq 0.025$.